ACS OMEGA

Open Access

http://pubs.acs.org/journal/acsodf

Article

Green Synthesis of ZnO Nanoparticles and Ag-Doped ZnO Nanocomposite Utilizing *Sansevieria trifasciata* for High-Performance Asymmetric Supercapacitors

Azam Raza,[⊥] Kaifee Sayeed,[⊥] Aeiman Naaz, Mohammad Muaz, Sk Najrul Islam, Sabiar Rahaman, Farasha Sama,* Kavita Pandey,* and Absar Ahmad*

Cite This: *ACS Omega* 2024, 9, 32444−32454

Read Online

ACCESS | Metrics & More | Article Recommendations | Supporting Information

ABSTRACT: This study provides a comprehensive analysis of a biofabricated nanomaterial derived from *Sansevieria trifasciata* root extract, evaluating its structural, morphological, and optical properties for use in asymmetric supercapacitors. The nanomaterial comprises pristine ZnO nanoparticles (ZnO NPs) and a 1% Ag-doped ZnO nanocomposite (Ag@ZnO NC), synthesized through a green-assisted sol−gel autocombustion method. Employing techniques such as X-ray diffraction, ultraviolet−visible near-infrared, scanning electron microscopy−energy-dispersive X-rayspectroscopy, Fourier transform infrared spectroscopy, Raman spectroscopy, and transmission electron microscopy, the study confirms a hexagonal wurtzite structure and nanocrystallites with spherical and hexagonal shapes (30 nm). Optical analysis reveals a red shift in the band gap with Ag doping, indicating improved conductivity. The material shows potential applications in solar cells, optoelectronics, spintronics, wastewater treatment, and high-performance asymmetric supercapacitors. Raman spectra validate the wurtzite phase and identify intrinsic defects. Electrochemical tests demonstrate remarkable supercapacitive behavior with a 94% capacitance retention after 10,000 cycles, highlighting its promise as advanced asymmetric supercapacitors.

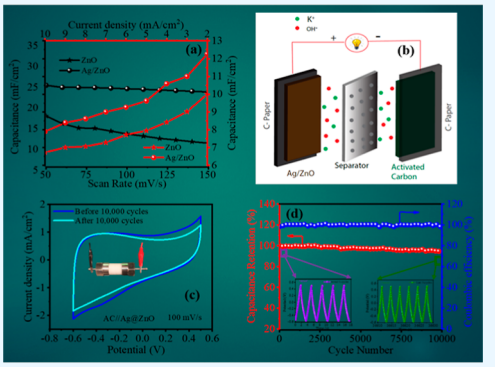

1. INTRODUCTION

In this cutting-edge era of science and technology, people seek new electronic devices with cutting-edge characteristics.[1] The development of new uses of large-band-gap-energy (E_g) semiconductor materials with prominent properties is encouraged viz ZnO,[2] TiO_2,[3] SnO_2,[4] NiO,[5] etc., are currently having attention due to large applications. Metal oxide (MO) semiconductors are widely used in many different applications, such as hybrid solar cells,[6] piezoelectric devices,[7] emission control,[8] LEDs,[9] UV shields,[10] gas-sensing devices,[11] temperature control paints,[12] supercapacitors,[13] and photocatalysis.[14] To repair our damaged environment and sustainably advance technology, semiconductor materials should be used more frequently. The development of advanced electronic features that are both gratifying and beneficial is necessary for the new world of electronic base systems.[15,16] In next-generation energy-storing devices, the supercapacitor has an effective energy-storage component for the output of high-power-demand applications.[17] To store energy, two types of supercapacitors can be distinguished by their primary properties: (i) electrochemical (EC) double-layer capacitors (EDLCs),[18] which use activated carbon, carbon aerogel, graphene, carbon nanotubes, etc., and (ii) pseudo capacitors,[19] which are used in NiO, MnO_2,[20] RuO_2,[21] ZnO, CoO,[22] etc. Because of their exceptional qualities, semiconductor oxides, including SnO_2, TiO_2, NiO, ZnO, and others, have been attracting the attention of researchers for usage in supercapacitors as electrode material.[23,24] ZnO is regarded as a cheap and environmentally friendly material used as an electrode for supercapacitor applications compared with other semiconductor oxides. There are several applications for supercapacitors, such as in hybrid vehicles, space or military technology, backup energy storage systems, and portable gadgets.[25] The characteristics and makeup of the electrolytes, current collectors, separators, and electrodes can all be changed to enhance the EC properties of supercapacitors. A transition metal can improve the EC performance in the crystal of the ZnO lattice.[23,26] Doping is a useful method for enhancing the chemical and physical characteristics of ZnO for a variety of applications. Numerous dopants, viz, Fe,[27] Bi,[28] Mn,[29] Cu,[30] etc., have been employed to control physiochemical properties by being incorporated into the crystal of ZnO

Received: December 16, 2023
Revised: February 27, 2024
Accepted: February 28, 2024
Published: July 16, 2024

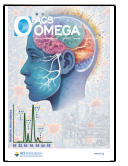

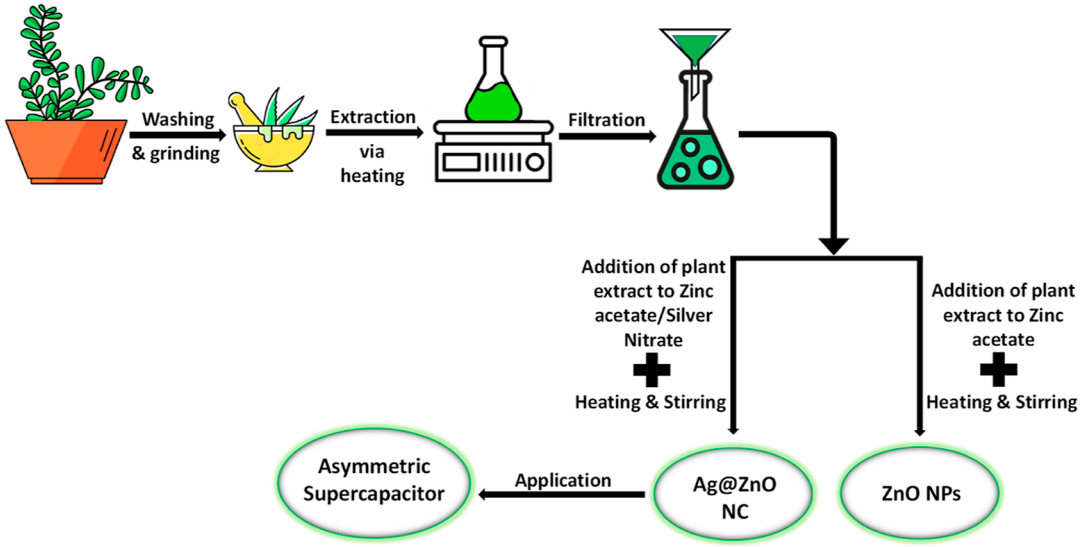

Figure 1. Schematic diagram for the synthesis of ZnO NPs and Ag@ZnO NC.

lattices. According to a survey of the literature, most research focuses on anticancer,[31] antifungal,[32] and antibacterial[33] applications since ZnO, a semiconductor material, is an excellent material for healthcare purposes.[34] We know that Ag performs well in electronic devices, by enhancing the EC performance,[35] thereby showing an abrupt increase in the capacitance values.[36] Various physical, chemical, and biological approaches have been developed for the fabrication of ZnO nanoparticles (ZnO NPs) and Ag-doped ZnO nanocomposite (ZnO NC), including hydrothermal,[37] sol−gel,[38] chemical vapor deposition,[39] sonochemical,[40] coprecipitation,[41] biological and microwave-assisted methods.[42] Biological methods have a number of advantages over other methods for synthesizing NPs, including increased yield, environmental friendliness, lower manufacturing costs, and high advantages in quality. The nano-based MO constituents have strong EC properties, including great stability, quick current response, low detection limit, and excellent repeatability, according to cyclic voltammetry (CV) investigations. Additionally, the projected values of the specific capacitance of the MO-based electrodes are higher than those obtained from experimental testing. There is hence a great chance of increasing the energy density of the MO-based electrodes. Different MO materials are used for PC applications.[43] These include ZnO/rGO 190.5 F/g[44] and Zr-doped ZnO 518 F/g.[45] ZnO is a cheap and environmentally favorable electrode material when compared with other metal oxides. Due to its superior physical and chemical characteristics, including enhanced EC stability and low toxicity, it is employed in a number of applications, including solar cells, photocatalytic activity, EC capacitors, batteries, and gas sensors.[46] ZnO is an n-type semiconductor with excellent optical and electrical performance and a big energy gap (E_g = 3.20 eV). It can withstand high-temperature doping and contact formation processes since it is resistant at those temperatures.[47] Depending on the surface shape, microstructure, and battery design, ZnO displays remarkable pseudocapacitive performance in a variety of topologies with a specific capacitance ranging from 5 to 500 F/g.[48,49] For the purpose of using supercapacitors, it is still possible to increase the capacitance of ZnO by adding impurities or creating a composite with carbon-based metals. Compared to pure metal, ZnO doped with cationic ions has a good EC performance. Researchers have found that cationic-doped ZnO performs better electrochemically than pure ZnO. According to Pallavolu et al.'s findings, Mo- and V-doped ZnO electrodes showed 555 and 585 F/g for 0.5 A/g, respectively.[50] Rashid et al. reported a value of 515 F/g at 2 mA/g for Mn-doped ZnO electrodes[45]

In the current study, using the green-aided sol−gel auto combustion approach, we have effectively synthesized a novel Ag-doped ZnO NC, which is made of ZnO and Ag doping in ratios such as $Ag_{0.01}ZnO_{0.99}$, for its usefulness in high-performance supercapacitor (SC) applications. Using XRD, SEM, EDX, UV−vis, and TEM, the morphology and structure of ZnO and $Ag_{0.01}ZnO_{0.99}$ NC have been studied. These findings demonstrated that the as-synthesized (Ag-doped ZnO) NC revealed extraordinary EC properties, including a tremendous areal capacitance compared with the pristine ZnO with superior charging/discharging capabilities and a very stable nature, indicating their suitability as electrode material in SC applications.

2. MATERIALS AND METHODS

2.1. Materials. In this experiment, all of the analytical-grade compounds were employed without further purification. The chemicals used in this experiment were zinc acetate dihydrate ($Zn(OAc)_2{\cdot}2H_2O$) (98.50%, Fisher Scientific), silver acetate ($AgNO_3$) (99.00%, Fisher Scientific), double-distilled water, Whatman filter paper no. 1, and root extract of *Sansevieria trifasciata*. For EC evaluation, carbon paper (~0.7 W) was used as the substrate. *N*-methyl-2-pyrrolidinone (NMP), PVA, and activated carbon purchased from Sigma-Aldrich Co., Ltd. were used as the solvent, binder, and conducting material, respectively. Double-deionized (DI) water obtained from a Sartorius mini plus UV was directly used in an aqueous electrolyte. Sodium sulfate procured from Merck was used as received to prepare 1 mole of a neutral-pH electrolyte.

2.2. Methods. ZnO NPs and Ag@ZnO NC were synthesized by using a biological approach. The sequential steps involved preparing plant extract: 30 g of *S. trifasciata* root was cut into small pieces, meticulously washed, and placed in a

https://doi.org/10.1021/acsomega.3c10060
ACS Omega 2024, 9, 32444−32454

conical flask. Subsequently, 200 mL of double-distilled water was added, and the solution was autoclaved for 30 min at 121 °C and 15 pounds per square inch of pressure. The mixture was filtered and cooled after being autoclaved, and the resultant plant extract was obtained. For the synthesis of pristine ZnO NPs, a plant extract of 25 mL was added to it in 100 mL of water containing a salt of zinc acetate. The precursor was kept in a magnetic stirrer at 250 rpm at 60 °C for 3 h until completely dry. Thereafter, it was calcined at 650 °C to get the ZnO NPs. 1% of a 0.1 M silver nitrate solution was mixed with the zinc acetate solution to achieve the doping of Ag ions into the zinc oxide structure. Specifically, 0.039 g of silver nitrate and 4.96 g of zinc acetate were dissolved in a 100 mL Erlenmeyer flask containing double-distilled water, to which 25 mL of the plant extract was added. Following the reaction, the precipitate formed as a result of the process was carefully dried by using a hot air oven. The dried precipitate was then ground to a suitable consistency using an agate mortar. The collected nanopowder, containing the Ag@ZnO NC, underwent a final calcination step at 350 °C for 3 h within a muffle furnace to get Ag@ZnO NC. Figure 1 shows a schematic diagram of biologically synthesized ZnO NPs and Ag@ ZnO NC.

A Rigaku Miniflex II desktop diffractometer (current of 15 mA, anode material Cu Kα, voltage of 30 kV, wavelength (Cu) 1.541838 Å) was used to determine the unit cell dimension and crystallinity phase. Optics involved beta filtering with graphite, automatic divergence slit, and monochromator in the 2θ range varying from 5 to 80° in 0.04° steps for the bio-fabricated samples. SEM (model no. JEM 2100, JEOL, Japan) was used for finding the surface morphology; for elemental identification, EDS was utilized attached with SEM. For analyzing the functional biomolecules present in the samples, FTIR spectroscopy was performed to detect the functional groups ranging from 400 to 4000 cm^{-1} (Make-PerkinElmer). Each sample was fabricated by mixing 200 mg of KBr (a background nonabsorbing media) with 2 mg of synthesized nanomaterial and applying high pressure to it. UV−visible NIR absorption spectra of ZnO NPs and Ag@ZnO NC were recorded between 200 and 800 nm using UV−visible NIR (Make-PerkinElmer, Model-Carry 5000) spectrophotometer. A Raman microscope with a 50× objective and a 532 nm He−Ne laser excitation source was used to gather the Raman spectra (Renishaw, RM-1000). The shape, particle size, crystalline structure, and surface morphology of NPs were investigated using TEM and selected area electron diffraction (SAED) patterns. ZnO NPs and Ag@ZnO NC powder samples were suspended in ethanol prior to precipitating on the grid. TEM (model no. JEM 2100, JEOL, Japan) was then used to scan the sample.

2.3. Electrode Preparation. The electrodes for EC studies were precisely created by using a series of methods. Initially, the as-synthesized active material, ZnO or Ag-doped ZnO, was mixed with activated carbon and poly(vinylidene fluoride) (PVDF) binder in a precise 8:1:1 weight ratio. To ensure proper mixing, this composite mixture was continuously ground for 1 h using a motor and pestle. Following that, the finely powdered mixture was combined with NMP, a high-purity solvent (99%, ACS reagent, Aldrich) that served as a dispersion agent. The resulting slurry was then placed on a magnetic stirrer to acquire a homogeneous slurry overnight. The homologous slurry was drop-cast onto carbon paper in an area of 1 × 1 cm^2 and the deposition was allowed to dry overnight in a vacuum oven at 80 °C until the solvent had completely evaporated. The resulting dry electrode was ready for EC experiments.

2.4. Device Fabrication. A Swagelok cell was used to make an asymmetric supercapacitor device. A device anode was created by combining pure activated carbon and PVDF in a 9:1 ratio. The cathode Ag-doped ZnO slurry was prepared in the same manner as described in Section 2.4. A circular, 13 mm diameter carbon paper was cut. The circular cut carbon paper was drop-casted with a slurry of activated carbon followed by Ag-doped ZnO. The resultant drop-cast electrode was dried overnight at 80 °C. As an electrolyte and separator, 1 M-KOH and Whatman filter paper were utilized. An asymmetric device was made after combining all together, as shown in the schematic.

3. RESULTS AND DISCUSSION

3.1. Powder X-ray Diffraction Studies. The diffraction patterns of pristine ZnO NPs and 1% Ag@ZnO NC are shown in Figure 2. The spectra demonstrate that the peaks are

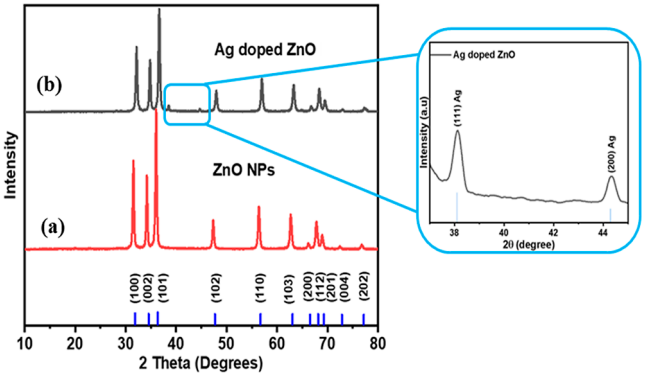

Figure 2. XRD pattern of (a) ZnO NPs and (b) Ag@ZnO NC.

polycrystalline and have a high degree of texture showing an intense peak at 2θ = 34.66° and a feeble peak at 2θ = 72.78°, which correspond to the plane (200) and its harmonic at (004) plane of hexagonal (wurtzite) structure confirming ZnO structure, according to JCPDS card file no. 00-36-1451.[51] This finding suggests that ZnO crystallites have a strong preference for *c*-axis orientation; when observed at 2θ = 36.69°, the third peak is equally quite modest when viewed from plane (101). Further, no other detected peaks correspond to secondary phases. The atomic radius of Ag is greater than that of Zn, so doping of Ag will increase the crystal size. Ag@ZnO NCs exhibit larger crystallites than pure ZnO NPs, which is explained by the difference in atomic radii; it is possible that smaller Zn atoms caused crystallites to aggregate and grow to the size of Ag atoms in the host lattice. From Figure 1, we can infer that Ag doping enhances the powder's crystallinity. The crystallite sizes of the nanomaterials were estimated using Scherrer's formula in eq 1[52]

$$D = \frac{0.9\lambda}{\beta \cos\theta} \quad (1)$$

where β is the peak's full width at half-maximum (fwhm), λ is the wavelength, θ is the Bragg angle, and D is the crystallite size.

3.2. FTIR Spectroscopy. Figure 3 displays the FTIR spectra of pristine and 1 wt % Ag@ZnO nanomaterials. Figure

https://doi.org/10.1021/acsomega.3c10060
ACS Omega 2024, 9, 32444−32454

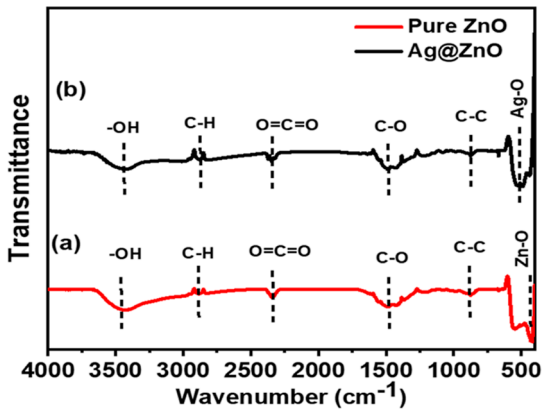

Figure 3. FTIR spectra of (a) ZnO NPs and (b) Ag@ZnO NC.

1 illustrates the wurtzite structures of pristine ZnO NPs and Ag-doped ZnO NC, which are further corroborated by using FTIR spectra. Additionally, FTIR spectra of ZnO NPs and Ag-doped ZnO NC were recorded between 400 and 4000 cm^{-1}. Zn−O and Ag−O stretching properties are attributed to the major bands at 425 and 514 cm^{-1},[53,54] respectively. At 880 and 885 cm^{-1}, the peak can be attributed to aromatic C═C stretching mode.[55,56] The absorption bands at 3445 and 3459 cm^{-1} arise due to the stretching of the mode O−H group;[57−59] it demonstrates that the ZnO nanostructure has absorbed a small amount of water. The peaks located at 2340 and 2364 cm^{-1} are due to the atmospheric CO_2 present in the instrument.[60,61] Stretching modes for ZnO NPs and Ag@ZnO NC of C−C and C═O are observed at 880, 885 and 1475, 1485 cm^{-1}, respectively.[58,62] The band between 2879 and 2885 cm^{-1} is attributable to vibrations caused by C−H stretching.[59,63,64] The host lattice's Ag doping is indicated by the peak shift from wavenumber 425 cm^{-1} to higher wavenumber 514 cm^{-1}.[65]

3.3. UV−Visible NIR Spectroscopy. Figure 4a displays the UV visible spectra of the Ag-doped and undoped ZnO NPs. The band gap of the synthesized ZnO NPs (3.13 eV) and Ag@ZnO NC (2.88 eV) corresponding to the absorption at 365 and 374 nm was calculated using the Kubelka−Munk plot (Figure 4b).[66−68] It can be easily seen that the maximum absorbance of Ag-doped ZnO lies in the visible region due to electron trapping. The Ag dopant decreases the band gap of the NPs thereby increasing the conductivity and improving the EC properties of the nanomaterial.[69,70]

3.4. Raman Analysis. The Raman spectrum is an important and adaptable diagnostic tool for investigating crystallization, structural flaws, and structural disorders in micro- and nanostructures. Raman spectra were used to examine the modes of vibrational characteristics of nanostructured ZnO. The $P6_3mc$ space group is occupied by ZnO NPs with hexagonal wurtzite structures. In the ideal ZnO crystal, only the optical phonons close to the Brillouin zone participate in first-order Raman scattering. The optical modes existing in wurtzite ZnO according to group theory are described in eq 2.[71]

$$\Gamma_{opt} = A_1 + 2B_2 + E_1 + 2E_2 \quad (2)$$

where, due to the macroscopic electric fields connected to the longitudinal optical (LO) phonons, the LO and the transverse optical (TO) branches of the A_1 and E_1 modes are both two polar branch components with distinct frequencies. The first-order Raman-active modes are A_1, E_1, and E_2. The B_1 modes, often known as silent modes, are defined by the Raman selection rule as typically being inactive in the Raman spectra. The Raman spectra of pure ZnO NPs are displayed in Figure 5.

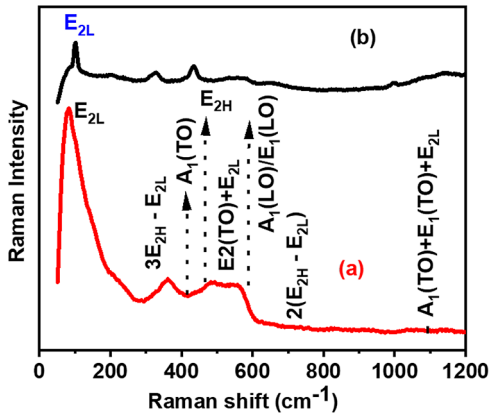

Figure 5. Raman spectra of (a) pure ZnO NPs and (b) Ag-doped ZnO NC.

The E2L, A1 (TO), E2H, and A1 (LO)/E1 (LO) basic phonon modes of hexagonal ZnO were measured at 100, 380, 441, and 586 cm^{-1}, respectively. The second-order phonon mode, designated 2E2L, is present at a wavelength of roughly 150 cm^{-1}. At 331, 508, 664, and 1065 cm^{-1}, which correspond

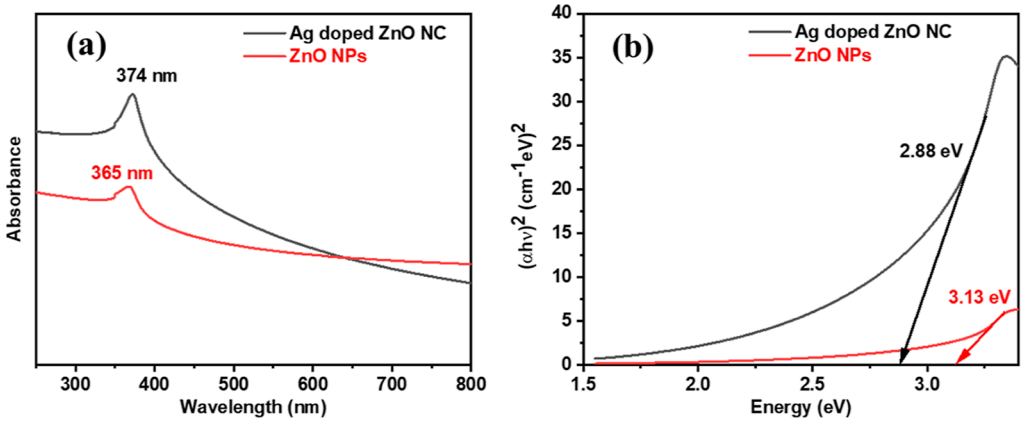

Figure 4. (a) UV visible absorption spectra of ZnO NPs and Ag@ZnO NC; (b) calculated band gap of ZnO NPs and Ag@ZnO NC.

https://doi.org/10.1021/acsomega.3c10060
ACS Omega 2024, 9, 32444−32454

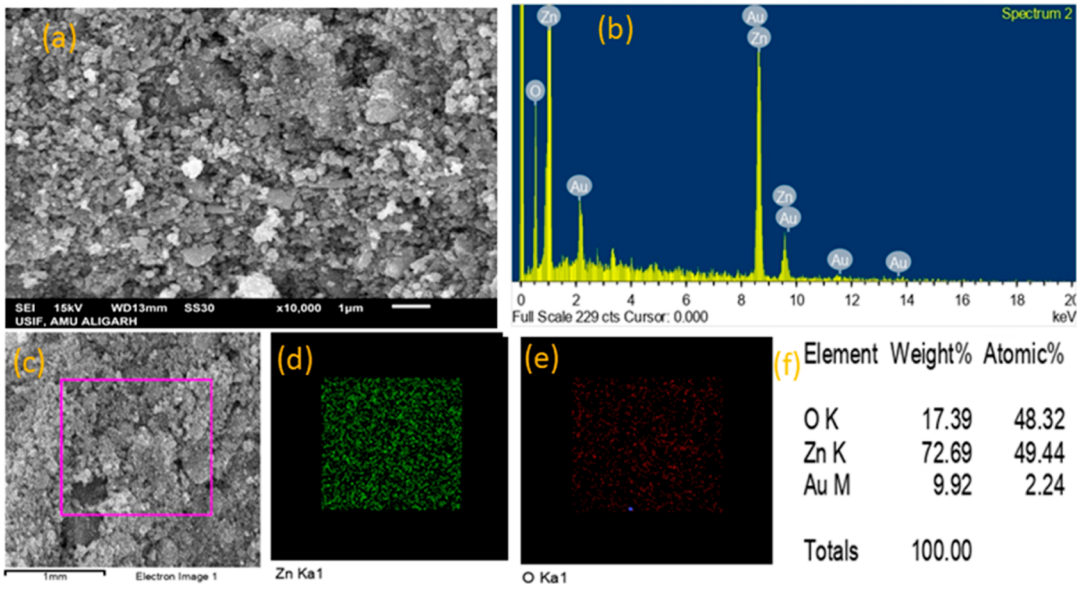

Figure 6. (a) SEM image of ZnO NPs and (b) corresponding EDX image confirming elemental composition. (c) Elemental mapping of NPs. (d) Elemental mapping of Zn. (e) Elemental mapping of O. (f) Elemental composition of NPs by weight (%) and atomic (%).

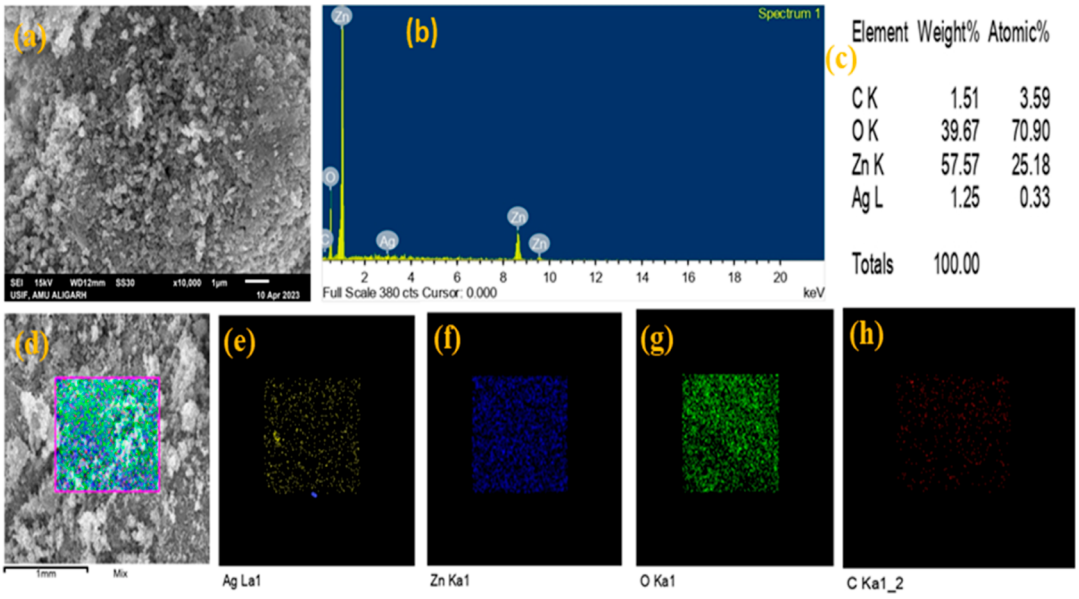

Figure 7. (a) SEM image of Ag@ZnO NC and (b) corresponding EDX image confirming elemental composition. (c) Elemental composition of Ag@ZnO NC by weight (%) and atomic (%). (d) Elemental mapping of Ag@ZnO NC. (e) elemental mapping of Ag. (f) Elemental mapping of Zn. (g) Elemental mapping of O. (h) Elemental mapping of C.

to the 3E2H−E2L, E1(TO) + E2L, 2(E2H−E2L), and A1(TO) + E1(TO) + E2L, respectively, the multiphonon scattering modes are presented. Additionally, at 1101 cm^{-1}, the acoustic combination of E2 and A1 may be heard. The Raman spectra of ZnO nanoparticles doped with 2 mM Ag are shown in Figure 5. The doping agent on the ZnO matrix dramatically alters the polar and nonpolar modes. The oxygen motion in the E2H mode is sensitive to internal stress and is a feature of hexagonal wurtzite ZnO nanostructures. A significant decrease in the intensity of Ag-doped samples in the E2H mode is caused by the breakdown of translational crystal symmetry brought on by the insertion of impurities and defects. Additionally, the polar mode of A1(LO)/E1(LO), which has a peak at about 570 cm^{-1} and is expanded and moved to lower energy, has been reported for Ag doping. Every phonon mode shift and broadening that the scattering contributions have produced outside the Brillouin zone center is represented. Typically, the defect complexes of zinc interstitial and oxygen vacancies in the ZnO lattice are represented by the A1 (LO)/E1 (LO) phonon mode. The addition of Ag ions to ZnO nanoparticles significantly boosts the intensity of the Ag-doped ZnO Raman peaks. The outcomes also provide additional evidence that ZnO nanoparticles included crystallization with minimal flaws brought on by Ag ions.[72]

3.5. SEM. Figure 6 depicts the rough surface morphology of ZnO NPs and Ag@ZnO NC obtained by using SEM. The samples were evaluated for size and form homogeneity (Figures 6a−f and 7 a−h). EDX analysis on the K and L lines was used to determine the topological characteristics and composition of the nanomaterial.

https://doi.org/10.1021/acsomega.3c10060
ACS Omega 2024, 9, 32444−32454

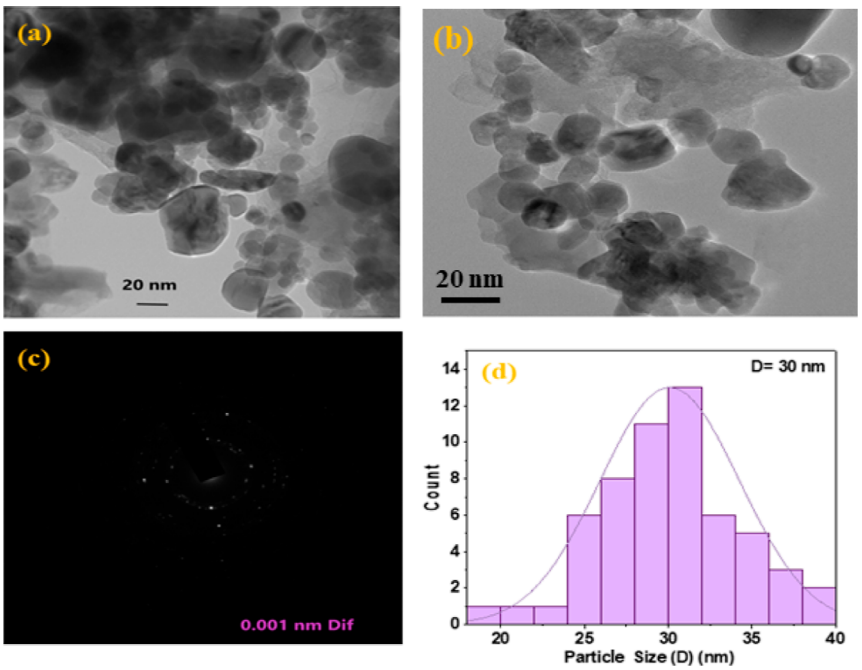

Figure 8. TEM images of Ag@ZnO NC confirming the formation at the nanoscale (a) 20 nm scale; (b) 20 nm scale; (c) SAED pattern with 0.001 nm diffraction; (d) average particle size calculated using Image J software from the TEM micrograph (a,b).

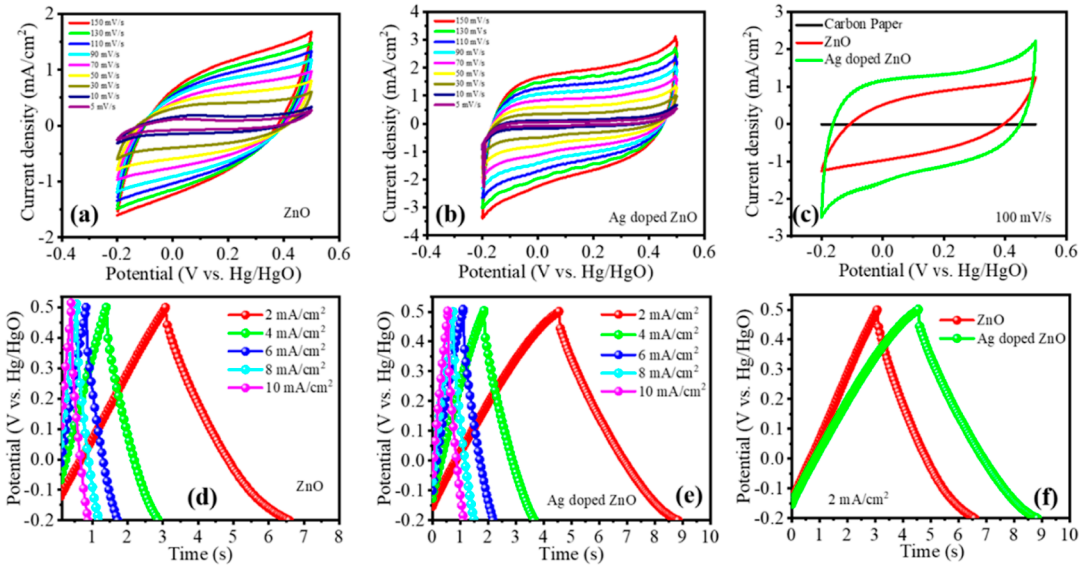

Figure 9. CV analysis of (a) ZnO at different scan rates (5−150 mV/s), (b) Ag-doped ZnO at different scan rates (5−150 mV/s), (c) comparison at 100 mV/s; galvanostatic charge−discharge analysis of (d) ZnO at different current densities (2−10 mA/cm^2), (e) Ag-doped ZnO at different current densities (2−10 mA/cm^2), and (f) comparison at 2 mA/cm^2.

Figures 6a−f and 7a−h depict the SEM images used to analyze the morphology of pure ZnO NPs and Ag@ZnO NC, respectively. Pure zinc oxide exhibits spherical particles, whereas zinc oxide that has been doped with 1% Ag displays agglomerated, larger spherical particles. XRD results acknowledge the recorded structures as a result. This indicated that particularly for measurements performed using the bracket sample holder, the XRD powder data may contain some preferred inclination effects. The crystallite size is a remarkable 1 μm, despite the fact that the particle size is bigger as a result of crystallite aggregation.

3.6. Transmission Electron Microscopy. TEM is typically valid for assessing the size, shape, and morphology of the nanoparticles, as well as for analytical characterization and imaging. Figure 8 displays a typical TEM picture of the Ag-doped ZnO NC. This image displayed particles with homogeneous, nearly identical diameters ranging from 20 to 35 nm (Figure 8a,b). The polycrystalline nature was depicted by the SAED pattern of TEM images which presents the concentric rings (Figure 8c). Furthermore, Figure 8c illustrates the NC information's SAED pattern: the circular white patches in the field of view exhibit the nanocrystalline particles, and the detailed investigations of SAED patterns explore the polycrystalline nature of Ag−ZnO NC of Ag and Zn in the same lattice plane [1 0 1]. However, they have different orientations in the plane.[70] TEM images confirmed the

https://doi.org/10.1021/acsomega.3c10060
ACS Omega 2024, 9, 32444−32454

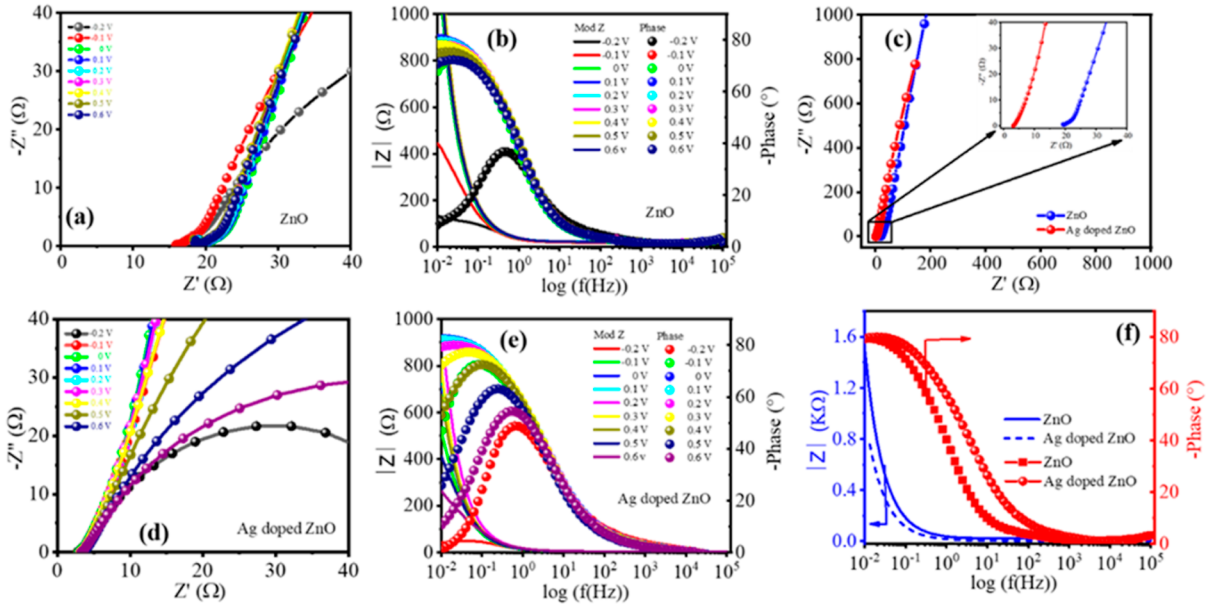

Figure 10. (a,b) Nyquist and Bode plot of pristine ZnO at various potentials; (d,e) Nyquist and Bode plot of Ag-doped ZnO at various potentials; (c,f) comparison of Nyquist and Bode plot of both ZnO and Ag-doped ZnO at OCP (open circuit potential).

formation of anisotropic nanoparticles, most of which were spherical and hexagonal in shape. Figure 8a,b was used to calculate the average particle size of Ag@ZnO NC using ImageJ software and was found to be 30 nm (Figure 8d).

4. EC ANALYSIS

4.1. CV Analysis. Numerous electrochemical investigations, including CV, galvanostatic charge−discharge, and electrochemical impedance spectroscopy (EIS), were used to study the EC properties of the synthesized ZnO and Ag-doped ZnO nanoparticles. For both ZnO and Ag-doped ZnO samples, the CV curves were taken at scan rates ranging from 5 to 150 mV/s. Figure 9a,b shows the CV curves of ZnO and Ag-doped ZnO nanostructures recorded at different scan rates ranging from 5 to 150 mV/s in the potential range of −0.2 to 0.5 V, respectively. Figure 9c shows the CV curves of the pure ZnO and Ag-doped ZnO samples at scan rates of 100 mV/s in the potential range of −0.2 to 0.5 V. The electrolyte remains stable within that particular region, also known as the stable EC potential window, which led to the selection of the range of −0.2 to 0.5 V. It can be concluded from the CV data in Figure 9a,b that the ZnO and Ag-doped ZnO nanostructure exhibit EDLC behavior. This conclusion was reached due to the rectangular shape of the curve and the lack of any discernible oxidation or reduction peaks, which confirm the EDLC behavior in both cases. It has been found that there is a positive correlation between the values of the scan rate and current density through our analysis of the CV curves for ZnO and Ag-doped ZnO nanoparticles. This result indicates that the capacitance performance of the nanoparticle electrodes is enhanced with an increase in the scan rate.

Compared with undoped ZnO, the area of the ZnO CV curve increases noticeably with the addition of Ag^+ ions to the lattice. Additionally, the rectangular shape of the CV curve is preserved even at higher scan rates. Compared to ZnO electrodes, the Ag-doped ZnO electrode has a higher areal capacitance (C_A), as shown by the larger area under the CV curve. The areal capacitance can be calculated using the following formula

$$C_A = \frac{\int i(v)\mathrm{d}V}{A\nu\Delta V}$$

where A is the geometric area of the working electrode, ν stands for scan rate, $\int i(v)\mathrm{d}V$ refers to the area under the CV curve, and ΔV stands for the potential window.[73,74] After the CV curves of ZnO NPs and Ag-doped ZnO electrodes were examined, it was found that the aerial capacitance (C_A) values were scan rate dependent. The C_A values of the ZnO NPs and Ag-doped ZnO electrodes were found to be 16.65 and 24.07 mF/cm^2, respectively, at a lower scan rate of 50 mV/s. The C_A values of the ZnO and Ag-doped ZnO electrodes decreased to 10.12 and 22.48 mF/cm^2, respectively, as the scan rate increased to 150 mV/s. This trend suggests that C_A values decrease with increasing scan rates due to a reduction in the interaction time between ions and the active material, resulting in a lower capacitance performance (Table S1 and Figure 9d). As a result, the scan rate and specific capacitance (Csp) have an opposite relationship.

4.2. Galvanostatic Charge−Discharge. Galvanostatic charge−discharge (GCD) curves are used to thoroughly characterize the EC behavior of ZnO NPs and Ag-doped ZnO electrodes by measuring the GCD curves within the EC potential window of −0.2 to 0.5 V. To precisely understand their EC properties, the GCD performance of ZnO NPs and Ag-doped ZnO NC is examined at various current densities ranging from 2 to 10 mA/cm^2. Figure 9d,e displays the GCD curves of ZnO NPs and Ag-doped ZnO electrodes at various current densities ranging from 2 to 10 mA/cm^2. The C_A values of ZnO and Ag-doped ZnO electrodes tend to decrease with increasing current density values, which is attributed to the inadequate redox reactions at electrode−electrolyte interfaces (Table S1).

Additionally, the curves obtained from the EC GCD analysis of ZnO and Ag-doped ZnO electrodes have a symmetrical triangle shape, further confirming the EDLC behavior of both

https://doi.org/10.1021/acsomega.3c10060
ACS Omega 2024, 9, 32444−32454

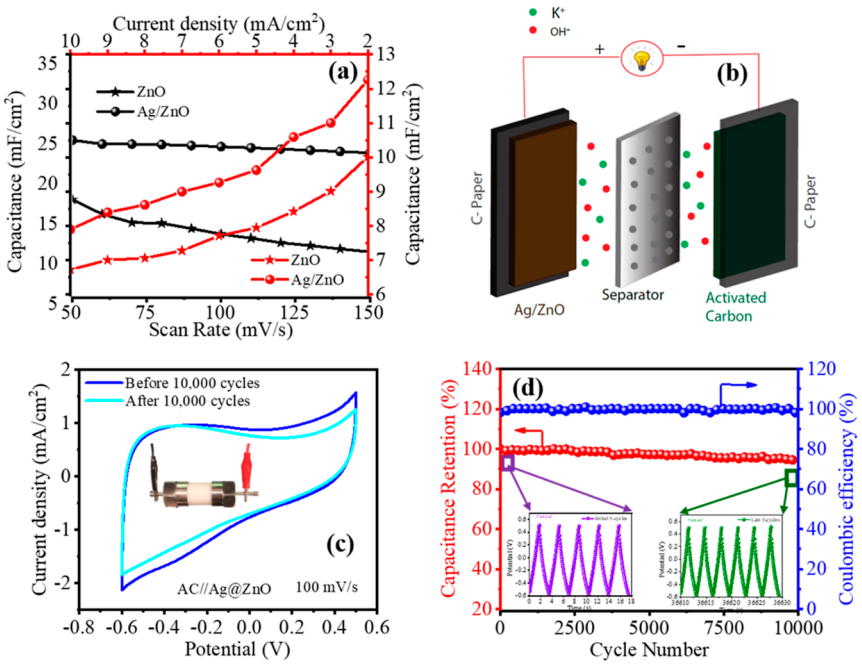

Figure 11. (a) Plot showing the variation of capacitance vs scan rate (black plot) and capacitance vs current density (red plot) for both ZnO and Ag-doped ZnO, (b) schematic of the asymmetric device consisting of activated carbon as an anode and Ag-doped ZnO as a cathode, (c) CV plot of the device at 100 mV/s before and after 10,000 cycles with the inset picture of a Swagelok cell, and (d) cyclic stability up to 10,000 cycles with the inset plots of first and last five cycles.

ZnO and Ag-doped ZnO electrodes (Figure 9d–f). The calculation of the average areal capacitance (C_A) of all ZnO and Ag-doped ZnO electrodes in the supercapacitors was carried out using the formula

$$C_A = \frac{I\Delta t}{A\Delta V}$$

where I is the constant current, Δt is the discharge time, A is the active area of the working electrode (1 × 1 cm^2), and ΔV is the potential window.[73]

The C_A values of ZnO and Ag-doped ZnO were 10.01 and 12.25 mF/cm^2 at a current density of 2 mA/cm^2 (Figure 9f). The GCD results reveal that the Ag-doped electrode shows better charging–discharging performance with enhanced capacitance.

4.3. EIS Study. EIS is a widely used technique to investigate the fundamental characteristics of electrode materials through the electrolyte ion transfer kinetics at various frequency ranges. EC impedance results were investigated using a frequency range of 0.01–10^5 Hz under an alternating potential of 10 mV, as shown in Figure 10a–f. Figure 10a–d displays a Nyquist plot of the EIS spectra for ZnO and Ag-doped electrodes. The solution resistance (R_s) and charge transfer resistance (R_{ct}) of EC reactions are calculated using the first and second intercepts with the real impedance axis in the plot above. The plot clearly shows that Ag-doped ZnO NC exhibits less solution resistance than pure ZnO. This demonstrates that Ag^+ doping improves the ability of the ZnO electrode to enhance the charge transfer performance.

The electrode diffusion rate is correlated with the impedance curve's slope at low frequencies.

The faster ion diffusion rate is associated with a steeper line at lower frequencies. Findings reveal that the Ag-doped ZnO electrode has a diffusion rate significantly higher than that of the ZnO.

Figure 10b–e displays a Bode plot for ZnO NPs and Ag-doped ZnO NC at various potentials ranging from −0.2 to 0.6 V. Compared to pure ZnO, the Ag-doped electrode has the quickest response time. Additionally, the phase angle in an Ag-doped ZnO electrode at lower frequencies approaches the ideal value of 90°, with a value of about 80°. This suggests that the sample has a strong capacitive property. Figure 10f depicts the Bode plot of pristine ZnO and Ag-doped samples at open circuit potential, clearly showing that Ag-doped ZnO has relatively less impedance modulus of the EC system. The phase angle has been found to be potential dependent, with a higher potential giving a larger phase angle, indicating a more significant capacitive contribution from the electrodes. This can be understood by the fact that an increase in the potential causes the frequency of the applied AC signal to increase proportionally. The supercapacitor's capacitive impedance component dominates at higher frequencies, causing the phase angle to close in on 90°, which is a sign of nearly ideal capacitive behavior.

The plot in Figure 11a shows how capacitance varies in relation to the scan rate and current density. The black plot illustrates the capacitance as a function of scan rate and provides information on how the capacitance varies with different scan rates. Additionally, the red plot illustrates the relation between capacitance and current density. According to these plots, the capacitance of the device decreases with increasing scan rate (as estimated from CV analysis) and current density (as determined from the GCD study) (Figure 11a and Table S1). Moreover, Ag-doped ZnO results were superior to those of pristine ZnO, which encouraged the use of Ag-doped ZnO in the fabrication of devices. Figure 11b illustrates a schematic representation of the asymmetric device, offering a visual understanding of its electrode composition.

https://doi.org/10.1021/acsomega.3c10060
ACS Omega 2024, 9, 32444–32454

The anode consists of an activated material, while the cathode comprises Ag-doped ZnO, with both drops cast on carbon paper. A cyclic stability test was performed to evaluate the asymmetric device's stability. Measurements were made at a current density of 5 mA/cm^2 to evaluate the device's performance over 10,000 cycles. Figure 11c,d displays the device's cyclic efficiency and highlights exciting results. Surprisingly, even after 10,000 cycles, the device shows excellent capacitance retention, at around 94%. This result indicates that the Ag-doped ZnO electrode performance has not substantially dropped in combination with activated carbon and exhibits excellent EC stability.

5. CONCLUSIONS

To test the feasibility as electrode materials in an asymmetric supercapacitor, pure ZnO and Ag-doped ZnO NC were made utilizing a simple green-assisted sol−gel autocombustion process. The structural characterizations of the Ag-doped ZnO NC, which enhanced the total electronic conductivity, included XRD, UV−vis, FTIR, SEM, and HR-TEM investigation. From the CV study, the C_A values of the ZnO NPs and Ag-doped ZnO electrodes were found to be 16.65 and 24.07 mF/cm^2, respectively, at a scan rate of 50 mV/s. Moreover, the GCD study shows that pure ZnO electrodes only have an arial capacitance of 10.01 mF/cm^2 at 2 mA/cm^2 and Ag-doped ZnO electrodes have a higher capacitance value of 12.25 mF/cm^2 at the same current density of 2 mA/cm^2. The data from CV and GCD illustrated its EDLC behavior, while EIS confirmed that its Ag-doped ZnO has a more conductive nature than pristine ZnO. Furthermore, Ag-doped ZnO was used as an electrode material in asymmetric supercapacitor devices. The capacity retention was found to be 94% after 10,000 cycles. Thus, Ag-doped ZnO NCs are a suitable option for supercapacitor applications based on the aforementioned findings. The distinctive Ag-doped ZnO electrodes demonstrate that there is a good electrode material for the next high-performance supercapacitor.

■ ASSOCIATED CONTENT

Supporting Information

The Supporting Information is available free of charge at https://pubs.acs.org/doi/10.1021/acsomega.3c10060.

Electrochemical data, i.e., variation of the areal capacitance of pristine and Ag-doped ZnO at different scan rates and current densities from CV and GCD studies, respectively (PDF)

■ AUTHOR INFORMATION

Corresponding Authors

Farasha Sama − *Interdisciplinary Nanotechnology Centre, Zakir Husain College of Engineering and Technology, Aligarh Muslim University, Aligarh 202002, India; Department of Industrial Chemistry, Aligarh Muslim University, Aligarh 202002, India;* orcid.org/0000-0003-1240-2667; Email: farashasamachem@gmail.com

Kavita Pandey − *Centre for Nano and Soft Matter Sciences (CeNS), Shivanapura, Bengaluru 562162, India; Academy of Scientific and Innovative Research (AcSIR), Ghaziabad 201002, India;* orcid.org/0000-0003-4426-1213; Email: kavitapandey@cens.res.in

Absar Ahmad − *Interdisciplinary Nanotechnology Centre, Zakir Husain College of Engineering and Technology, Aligarh Muslim University, Aligarh 202002, India;* orcid.org/0000-0002-2708-238X; Email: aahmad786in@gmail.com

Authors

Azam Raza − *Interdisciplinary Nanotechnology Centre, Zakir Husain College of Engineering and Technology, Aligarh Muslim University, Aligarh 202002, India;* orcid.org/0000-0001-6847-6441

Kaifee Sayeed − *Centre for Nano and Soft Matter Sciences (CeNS), Shivanapura, Bengaluru 562162, India*

Aeiman Naaz − *Interdisciplinary Nanotechnology Centre, Zakir Husain College of Engineering and Technology, Aligarh Muslim University, Aligarh 202002, India*

Mohammad Muaz − *Interdisciplinary Nanotechnology Centre, Zakir Husain College of Engineering and Technology, Aligarh Muslim University, Aligarh 202002, India*

Sk Najrul Islam − *Interdisciplinary Nanotechnology Centre, Zakir Husain College of Engineering and Technology, Aligarh Muslim University, Aligarh 202002, India*

Sabiar Rahaman − *Centre for Nano and Soft Matter Sciences (CeNS), Shivanapura, Bengaluru 562162, India;* orcid.org/0000-0001-6789-6540

Complete contact information is available at: https://pubs.acs.org/10.1021/acsomega.3c10060

Author Contributions

⊥A.R. and K.S. contributed equally.

Notes

The authors declare no competing financial interest.

■ ACKNOWLEDGMENTS

We acknowledge the Department of Biotechnology (DBT), Government of India, for setting up a Centre of Excellence (COE, BT/PR1-3584/COE/34/29/2015) at Interdisciplinary Nanotechnology Centre (INC), Aligarh Muslim University, AMU, Aligarh, UP-202002, India. We thank Khateeb and Asif of INC for their technical assistance. Kaifee Sayeed and Kavita Pandey greatly acknowledge funding received from the Science and Engineering Research Board (SERB) through SCP/2022/000943 and CRG/2022/006798. The authors also acknowledge the Central Research Facilities, Centre for Nano and Soft Matter Sciences (CeNS), Bengaluru, for providing all research facilities. Kaifee Sayeed acknowledges the Council of Scientific and Industrial Research (CSIR) for funding (09/1243(13523)/2022-EMR-I). Sabiar Rahaman acknowledges the research fellowship from the CeNS, Bengaluru.

■ REFERENCES

(1) Ayoub, I.; Kumar, V.; Abolhassani, R.; Sehgal, R.; Sharma, V.; Sehgal, R.; Swart, H. C.; Mishra, Y. K. Advances in ZnO: Manipulation of defects for enhancing their technological potentials. *Nanotechnol. Rev.* **2022**, *11* (1), 575−619.

(2) Zhao, X.; Li, Q.; Xu, L.; Zhang, Z.; Kang, Z.; Liao, Q.; Zhang, Y. Interface engineering in 1D ZnO-based heterostructures for photoelectrical devices. *Adv. Funct. Mater.* **2022**, *32* (11), 2106887.

(3) Fan, Q.; Wang, T.; Fan, W.; Xu, L. Recyclable visible-light photocatalytic composite materials based on tubular Au/TiO2/SiO2 ternary nanocomposites for removal of organic pollutants from water. *Compos. Commun.* **2022**, *32*, 101154.

(4) Kiani, M. S.; Sadirkhanov, Z. T.; Kakimov, A. G.; Parkhomenko, H. P.; Ng, A.; Jumabekov, A. N. Solution-Processed SnO2 Quantum Dots for the Electron Transport Layer of Flexible and Printed Perovskite Solar Cells. *Nanomaterials* **2022**, *12* (15), 2615.

(5) Tiwari, N.; Arianita Dewi, H.; Erdenebileg, E.; Narayan Chauhan, R.; Mathews, N.; Mhaisalkar, S.; Bruno, A. Advances and Potentials of $NiO_{<i>x</i>}$ Surface Treatments for p−i−n Perovskite Solar Cells. *Sol. RRL* **2022**, *6* (3), 2100700.
(6) Agrawal, A.; Siddiqui, S. A.; Soni, A.; Sharma, G. D. Advancements, frontiers and analysis of metal oxide semiconductor, dye, electrolyte and counter electrode of dye sensitized solar cell. *Sol. Energy* **2022**, *233*, 378−407.
(7) Jiang, Z.; Tan, X.; Huang, Y. Piezoelectric effect enhanced photocatalysis in environmental remediation: State-of-the-art techniques and future scenarios. *Sci. Total Environ.* **2022**, *806*, 150924.
(8) Mirzaei, A.; Ansari, H. R.; Shahbaz, M.; Kim, J. Y.; Kim, H. W.; Kim, S. S. Metal oxide semiconductor nanostructure gas sensors with different morphologies. *Chemosensors* **2022**, *10* (7), 289.
(9) Zheng, X.; etal. P-10: Emit Signals Reused Gate Driver Design for Ultra-Narrow-Bezel Micro-LED Display Based on Metal-Oxide TFTs. *SID Symposium Digest of Technical Papers*; Wiley Online Library, 2022.
(10) Farris, P. K.; Valacchi, G. Ultraviolet light protection: is it really enough? *Antioxidants* **2022**, *11* (8), 1484.
(11) Jin, T.; Ko Park, S. H.; Fang, D.-W. Highly-stable flexible pressure sensor using piezoelectric polymer film on metal oxide TFT. *RSC Adv.* **2022**, *12* (33), 21014−21021.
(12) Xie, H.; Li, Z.; Cheng, L.; Haidry, A. A.; Tao, J.; Xu, Y.; Xu, K.; Ou, J. Z. Recent advances in the fabrication of 2D metal oxides. *Iscience* **2022**, *25* (1), 103598.
(13) Zhai, Z.; Zhang, L.; Du, T.; Ren, B.; Xu, Y.; Wang, S.; Miao, J.; Liu, Z. A review of carbon materials for supercapacitors. *Mater. Des.* **2022**, *221*, 111017.
(14) Qumar, U.; Hassan, J. Z.; Bhatti, R. A.; Raza, A.; Nazir, G.; Nabgan, W.; Ikram, M. Photocatalysis vs adsorption by metal oxide nanoparticles. *J. Mater. Sci. Technol.* **2022**, *131*, 122−166.
(15) Emadi, A.; Williamson, S. S.; Khaligh, A. Power electronics intensive solutions for advanced electric, hybrid electric, and fuel cell vehicular power systems. *IEEE Trans. Power Electron.* **2006**, *21* (3), 567−577.
(16) Huang, J.; Xie, Y.; You, Y.; Yuan, J.; Xu, Q.; Xie, H.; Chen, Y. Rational design of electrode materials for advanced supercapacitors: from lab research to commercialization. *Adv. Funct. Mater.* **2023**, *33* (14), 2213095.
(17) Jan, W.; Khan, A. D.; Iftikhar, F. J.; Ali, G. Recent advancements and challenges in deploying lithium sulfur batteries as economical energy storage devices. *J. Energy Storage* **2023**, *72*, 108559.
(18) Martín-Illán, J. Á.; Sierra, L.; Ocón, P.; Zamora, F. Electrochemical Double-Layer Capacitor based on Carbon@ Covalent Organic Framework Aerogels. *Angew. Chem., Int. Ed.* **2022**, *61* (48), No. e202213106.
(19) Yamada, S. A Transient Pseudo-Capacitor Using a Bioderived Ionic Liquid with Na Ions. *Small* **2023**, *19* (15), 2205598.
(20) Barclay, M.; Firestein, K.; Wang, X.; Motta, N.; Dubal, D.; Ostrikov, K. Plasma-activated water for improved intercalation and pseudocapacitance of MnO2 supercapacitor electrodes. *Mater. Today Sustain.* **2023**, *22*, 100388.
(21) Sinha, P.; Kar, K. K. A flexible and high energy density-hydrous RuO2 and keratin-derived renewable carbon composite-based asymmetric supercapacitor in redox-mediated electrolytes. *Electrochim. Acta* **2022**, *435*, 141368.
(22) Jiao, Z.; Chen, Y.; Du, M.; Demir, M.; Yan, F.; Xia, W.; Zhang, Y.; Wang, C.; Gu, M.; Zhang, X.; et al. 3D hollow NiCo LDH nanocages anchored on 3D CoO sea urchin-like microspheres: A novel 3D/3D structure for hybrid supercapacitor electrodes. *J. Colloid Interface Sci.* **2023**, *633*, 723−736.
(23) Altaf, C. T.; Coskun, O.; Kumtepe, A.; Rostas, A. M.; Iatsunskyi, I.; Coy, E.; Erdem, E.; Sankir, M.; Sankir, N. D. Photo-supercapacitors based on nanoscaled ZnO. *Sci. Rep.* **2022**, *12* (1), 11487.
(24) Anwar, M. I.; Asad, M.; Ma, L.; Zhang, W.; Abbas, A.; Khan, M. Y.; Zeeshan, M.; Khatoon, A.; Gao, R.; Manzoor, S.; et al. Nitrogenous MOFs and their composites as high-performance electrode material for supercapacitors: Recent advances and perspectives. *Coord. Chem. Rev.* **2023**, *478*, 214967.
(25) Hussain, A.; Oves, M.; Alajmi, M. F.; Hussain, I.; Amir, S.; Ahmed, J.; Rehman, M. T.; El-Seedi, H. R.; Ali, I. Biogenesis of ZnO nanoparticles using Pandanus odorifer leaf extract: anticancer and antimicrobial activities. *RSC Adv.* **2019**, *9* (27), 15357−15369.
(26) Ahmar Rauf, M.; Oves, M.; Ur Rehman, F.; Rauf Khan, A.; Husain, N. Bougainvillea flower extract mediated zinc oxide's nanomaterials for antimicrobial and anticancer activity. *Biomed. Pharmacother.* **2019**, *116*, 108983.
(27) Dar, M. A.; Govindarajan, D.; Batoo, K. M.; Siva, C. Supercapacitor and magnetic properties of Fe doped SnS nanoparticles synthesized through solvothermal method. *J. Energy Storage* **2022**, *52*, 105034.
(28) Shenoy, U. S.; Bhat, D. K.; Bhat, D. K. Probing of Bi doped GeTe thermoelectrics leads to revelation of resonant states. *J. Alloys Compd.* **2022**, *921*, 165965.
(29) Xu, T.; Du, F.; Wu, L.; Fan, Z.; Shen, L.; Zheng, J. Boosting the electrochemical performance of LiNiO2 by extra low content of Mn-doping and its mechanism. *Electrochim. Acta* **2022**, *417*, 140345.
(30) Agboola, P. O.; Shakir, I.; Almutairi, Z. A.; Shar, S. S. Hydrothermal synthesis of Cu-doped CoS2@ NF as high performance binder free electrode material for supercapacitors applications. *Ceram. Int.* **2022**, *48* (6), 8509−8516.
(31) Abass Sofi, M.; Sunitha, S.; Ashaq Sofi, M.; Khadheer Pasha, S.; Choi, D. An overview of antimicrobial and anticancer potential of silver nanoparticles. *J. King Saud Univ. Sci.* **2022**, *34* (2), 101791.
(32) Lyagin, I.; Aslanli, A.; Domnin, M.; Stepanov, N.; Senko, O.; Maslova, O.; Efremenko, E. Metal nanomaterials and hydrolytic enzyme-based formulations for improved antifungal activity. *Int. J. Mol. Sci.* **2023**, *24* (14), 11359.
(33) Franco, D.; Calabrese, G.; Guglielmino, S. P. P.; Conoci, S. Metal-based nanoparticles: Antibacterial mechanisms and biomedical application. *Microorganisms* **2022**, *10* (9), 1778.
(34) Lawal, I. O.; Rafiu, B. O.; Ale, J. E.; Majebi, O. E.; Aremu, A. O. Ethnobotanical survey of local flora used for medicinal purposes among indigenous people in five areas in Lagos State, Nigeria. *Plants* **2022**, *11* (5), 633.
(35) Nethaji, P.; Senthil Kumar, P. V-Ag doped ZnO nanorod as high-performance electrode material for supercapacitors with enhanced specific capacitance and cycling stability. *Chem. Eng. Res. Des.* **2022**, *178*, 356−368.
(36) Rajkumar, S.; Subha, R.; Gowri, S.; Bella, A.; Merlin, J. P. Enhanced electrochemical performance of aminophenol-modified ZnO as electrode material for supercapacitors. *Ionics* **2022**, *28*, 859−869.
(37) Asjadi, F.; Yaghoobi, M. Characterization and dye removal capacity of green hydrothermal synthesized ZnO nanoparticles. *Ceram. Int.* **2022**, *48* (18), 27027−27038.
(38) Bhosale, A.; Kadam, J.; Gade, T.; Sonawane, K.; Garadkar, K. Efficient photodegradation of methyl orange and bactericidal activity of Ag doped ZnO nanoparticles. *J. Indian Chem. Soc.* **2023**, *100* (2), 100920.
(39) Abbas, A.; Mansoor, S.; Nawaz, M. H.; Chaudhry, A. A.; Ijaz, K.; Riaz, S.; Hayat, A. Growth of diazonium-functionalized ZnO nanoflakes on flexible carbon cloth for electrochemical sensing of acetone in the liquid phase. *RSC Adv.* **2023**, *13* (17), 11537−11545.
(40) Hu, X.; Zhang, Y.; Zhang, J.; Yang, H.; Wang, F.; Bin Fei; Noor, N. Sonochemically-coated transparent wood with ZnO: Passive radiative cooling materials for energy saving applications. *Renewable Energy* **2022**, *193*, 398−406.
(41) Pavithra, M.; Jessie Raj, M. Synthesis of ultrasonic assisted co-precipitated Ag/ZnO nanorods and their profound anti-liver cancer and antibacterial properties. *Mater. Sci. Eng. B* **2022**, *278*, 115653.
(42) Porrawatkul, P.; Pimsen, R.; Kuyyogsuy, A.; Teppaya, N.; Noypha, A.; Chanthai, S.; Nuengmatcha, P. Microwave-assisted synthesis of Ag/ZnO nanoparticles using Averrhoa carambola fruit extract as the reducing agent and their application in cotton fabrics

https://doi.org/10.1021/acsomega.3c10060
ACS Omega 2024, 9, 32444−32454

with antibacterial and UV-protection properties. *RSC Adv.* **2022**, *12* (24), 15008−15019.
(43) Sivakumar, P.; Kulandaivel, L.; Park, J.; Raj, C. J.; Ramesh, R.; Jung, H. Rational design and fabrication of one-dimensional hollow cuboid-like FeMoO4 architecture as a high performance electrode for hybrid supercapacitor. *Ceram. Int.* **2022**, *48* (19), 29144−29151.
(44) Shaheen, I.; Hussain, I.; Zahra, T.; Memon, R.; Alothman, A. A.; Ouladsmane, M.; Qureshi, A.; Niazi, J. H. Electrophoretic Fabrication of ZnO/CuO and ZnO/CuO/rGO Heterostructures-based Thin Films as Environmental Benign Flexible Electrode for Supercapacitor. *Chemosphere* **2023**, *322*, 138149.
(45) Nethaji, P.; Senthil Kumar, P. V-Ag doped ZnO nanorod as high-performance electrode material for supercapacitors with enhanced specific capacitance and cycling stability. *Chem. Eng. Res. Des.* **2022**, *178*, 356−368.
(46) Bu, F.; Zhou, W.; Xu, Y.; Du, Y.; Guan, C.; Huang, W. Recent developments of advanced micro-supercapacitors: design, fabrication and applications. *npj Flexible Electron.* **2020**, *4* (1), 31.
(47) Lamba, P.; Singh, P.; Singh, P.; Singh, P.; Bharti; Kumar, A.; Gupta, M.; Kumar, Y. Recent advancements in supercapacitors based on different electrode materials: Classifications, synthesis methods and comparative performance. *J. Energy Storage* **2022**, *48*, 103871.
(48) Sahu, J.; Kumar, S.; Ahmed, F.; Alvi, P.; Dalela, B.; Phase, D.; Gupta, M.; Dalela, S. Electrochemical and electronic structure properties of high-performance supercapacitor based on Nd-doped ZnO nanoparticles. *J. Energy Storage* **2023**, *59*, 106499.
(49) Üstün, B.; Aydın, H.; Koç, S. N.; Kurtan, Ü. Amorphous ZnO@S-doped carbon composite nanofiber for use in asymmetric supercapacitors. *Diamond Relat. Mater.* **2023**, *136*, 110048.
(50) Pallavolu, M. R.; Gaddam, N.; Banerjee, A. N.; Nallapureddy, R. R.; Joo, S. W. Superior energy-power performance of N-doped carbon nano-onions-based asymmetric and symmetric supercapacitor devices. *Int. J. Energy Res.* **2022**, *46* (2), 1234−1249.
(51) Gupta, P.; Joshi, B. Investigation of band alignment variations in CuZnO/ZnO heterostructures: Synchrotron-based valence band spectroscopy. *Vacuum* **2023**, *216*, 112455.
(52) Mahalakshmi, A.; et al. Synthesis of ZnO nanoparticles and its characterization techniques using XRD and FTIR *AIP Conference Proceedings*; AIP Publishing, 2022.
(53) Khan, A.; Kamal, T.; Saad, M.; Ameen, F.; Bhat, S. A.; Ahamad Khan, M.; Rahman, F. Synthesis and antibacterial activity of nanoenhanced conjugate of Ag-doped ZnO nanorods with graphene oxide. *Spectrochim. Acta, Part A* **2023**, *290*, 122296.
(54) Islam, S.; Naqvi, S. M. A.; Parveen, S.; Ahmad, A. Application of mycogenic silver/silver oxide nanoparticles in electrochemical glucose sensing; alongside their catalytic and antimicrobial activity. *3 Biotech* **2021**, *11*, 342.
(55) Shi, H.; Wang, H.; Zhou, Y.; Li, J.; Zhai, P.; Li, X.; Gurzadyan, G. G.; Hou, J.; Yang, H.; Guo, X. Atomically Dispersed Indium-Copper Dual-Metal Active Sites Promoting C- C Coupling for CO2 Photoreduction to Ethanol. *Angew. Chem.* **2022**, *134* (40), No. e202208904.
(56) Najrul Islam, S.; Muaz, M.; Rizvi, A. H.; Parveen, S.; Mohd Adnan Naqvi, S.; Raza, A.; Ansari, M. M.; Ramchandra Patil, C.; Ahmad, A. Sustainable production of wurtzite Zinc Sulphide nanocatalyst for detoxification of hexavalent chromium in water and their antibacterial and antioxidant activity. *Inorg. Chem. Commun.* **2023**, *152*, 110692.
(57) Raza, A.; Shoeb, M.; Mashkoor, F.; Rahaman, S.; Mobin, M.; Jeong, C.; Yusuf Ansari, M.; Ahmad, A. Phoenix dactylifera mediated green synthesis of Mn doped ZnO nanoparticles and its adsorption performance for methyl orange dye removal: A comparative study. *Mater. Chem. Phys.* **2022**, *286*, 126173.
(58) Islam, S. N.; Naqvi, S. M. A.; Raza, A.; Jaiswal, A.; Singh, A. K.; Dixit, M.; Barnwal, A.; Gambhir, S.; Ahmad, A. Mycosynthesis of highly fluorescent selenium nanoparticles from Fusarium oxysporum, their antifungal activity against black fungus Aspergillus niger, and in-vivo biodistribution studies. *3 Biotech* **2022**, *12* (11), 309.
(59) Khalilullah, A.; Sayeed, K.; Uddin, I. Bioinspired GO/Au nanocomposite synthesis: Characteristics and use as a high-performance dielectric material in nanoelectronics. *South Afr. J. Bot.* **2022**, *151*, 66−73.
(60) Zhang, S.; Yu, S.; Li, Q.; Mohamed, B. A.; Zhang, Y.; Zhou, H. Insight into the relationship between CO2 gasification characteristics and char structure of biomass. *Biomass Bioenergy* **2022**, *163*, 106537.
(61) Islam, S.; Naqvi, S. M. A.; Parveen, S.; Ahmad, A. Endophytic fungus-assisted biosynthesis, characterization and solar photocatalytic activity evaluation of nitrogen-doped Co3O4 nanoparticles. *Appl. Nanosci.* **2021**, *11*, 1651−1659.
(62) Jayasheela, K.; Nagabalasubramanian, P. B.; Periandy, S. Conformational & spectroscopic characterization, charge analysis and molecular docking profiles of chromone-3-carboxylic acid using a quantum hybrid computational method. *Heliyon* **2020**, *6*, No. e04775.
(63) Mukherjee, G.; Biradha, K. 1D, 2D and 3D coordination polymers of 1,3-phenylene diisonicotinate with Cu(I)/Cu(II): Cu2I2 building block, anion influence and guest inclusions. *CrystEngComm* **2014**, *16*, 4701−4705.
(64) Islam, S. N.; Raza, A.; Naqvi, S.; Parveen, S.; Ahmad, A. Unveiling the antisporulant activity of mycosynthesized gold-selenide nanoparticles against black fungus Aspergillus niger. *Surface. Interfac.* **2022**, *29*, 101769.
(65) Gayathri, S.; et al. Investigation of physicochemical properties of Ag doped ZnO nanoparticles prepared by chemical route. *Appl. Sci. Lett.* **2015**, *1*, 8.
(66) Subha, P.; Jayaraj, M. Enhanced room temperature gas sensing properties of low temperature solution processed ZnO/CuO heterojunction. *BMC Chem.* **2019**, *13*, 4.
(67) Jayaseelan, C.; Rahuman, A. A.; Kirthi, A. V.; Marimuthu, S.; Santhoshkumar, T.; Bagavan, A.; Gaurav, K.; Karthik, L.; Rao, K. B. Novel microbial route to synthesize ZnO nanoparticles using Aeromonas hydrophila and their activity against pathogenic bacteria and fungi. *Spectrochim. Acta, Part A* **2012**, *90*, 78−84.
(68) Wagh, S. S.; Kadam, V. S.; Jagtap, C. V.; Salunkhe, D. B.; Patil, R. S.; Pathan, H. M.; Patole, S. P. Comparative Studies on Synthesis, Characterization and Photocatalytic Activity of Ag Doped ZnO Nanoparticles. *ACS Omega* **2023**, *8* (8), 7779−7790.
(69) Rafique, S.; Kasi, A. K.; Kasi, J. K.; Aminullah; Bokhari, M.; Shakoor, Z. Fabrication of silver-doped zinc oxide nanorods piezoelectric nanogenerator on cotton fabric to utilize and optimize the charging system. *Nanomater. Nanotechnol.* **2020**, *10*, 184798041989574.
(70) Sagadevan, S.; Pal, K.; Chowdhury, Z. Z.; Hoque, M. E. Structural, dielectric and optical investigation of chemically synthesized Ag-doped ZnO nanoparticles composites. *J. Sol-Gel Sci. Technol.* **2017**, *83*, 394−404.
(71) Zeferino, R.; Flores, M. B.; Pal, U. Photoluminescence and Raman Scattering in Ag-doped ZnO Nanoparticles. *J. Appl. Phys.* **2011**, *109*, 014308.
(72) Herzi, A.; Sebais, M.; Boudine, B.; Halimi, O.; Rahal, B.; Guerbous, L. Fabrication and Characterization of Highly Textured Thin Films of Undoped and Ag-Doped ZnO. *Acta Phys. Pol., A* **2019**, *135*, 526−531.
(73) Rahaman, S.; Kanakala, M. B.; Waldiya, M.; Sadhanala, A.; Yelamaggad, C. V.; Pandey, K. Scalable novel lanthanide-ligand complex for robust flexible micro-supercapacitors. *J. Power Sources* **2023**, *564*, 232801.
(74) Hu, Z.; He, T.; Li, W.; Huang, J.; Zhang, A.; Wang, S.; Zhou, W.; Xu, J. Controllable 3D Flower-Like Ag-CF Electrodes as Flexible Marine Electric Field Sensors with High Stability. *Inorg. Chem.* **2023**, *62* (8), 3541−3554.

https://doi.org/10.1021/acsomega.3c10060
ACS Omega 2024, 9, 32444−32454